Life Cycle of Precipitating Cloud Systems from Synergistic Satellite Observations: Evolution of Macrophysical Properties and Precipitation Statistics from Geostationary Cloud Tracking and GPM Active and Passive Microwave Measurements

Clément Guilloteau[1,*] and Efi Foufoula-Georgiou[1,2]

[1] Department of civil and environmental engineering, University of California Irvine

[2] Department of Earth system science, University of California Irvine

* corresponding author, cguillot@uci.edu

Abstract

Observations of clouds and precipitation in the microwave domain from the active radar (DPR) and the passive imager (GMI) onboard the GPM Core Observatory satellite are used in synergy with cloud tracking information derived from infrared imagery from the GOES-13 and Meteosat-7 geostationary satellites for analysis of the life cycle of precipitating cloud systems, in terms of temporal evolution of their macro-physical characteristics, in several oceanic and continental regions of the Tropics. The life cycle of each one of the several hundred thousand cloud systems tracked during the two-year (2015-2016) analysis period is divided into five equal-duration stages between initiation and dissipation. The average cloud size, precipitation intensity, precipitation top height, and convective and stratiform precipitating fractions are documented at each stage of the life cycle for different cloud categories (based upon lifetime duration). The average life cycle dynamics is found remarkably homogeneous across the different regions and is consistent with previous studies: systems peak in size around mid-life; precipitation intensity and convective fraction tend to decrease continuously from the initiation stage to the dissipation. Over the three continental regions, Amazonia, Central Africa and Sahel, at the early stages of clouds' life cycle, precipitation estimates from the passive GMI instrument are systematically found to be 15 to 40% lower than active radar estimates. By highlighting stage-dependent biases in state-of-the-art passive microwave precipitation estimates over land we demonstrate the potential usefulness of cloud tracking information for improving retrievals, and suggest new directions for the synergistic use of geostationary and low-Earth-orbit satellite observations.

1) Introduction

The observation of clouds from satellites has a relatively long history. The first meteorological satellite, Vanguard-2, carrying a cloud optical scanner [Hanel et al. 1960], was launched by the United States in 1959, less than two years after the first-ever artificial satellite, Sputnik-1, was put into orbit by the USSR. Since then, satellite radiometric measurements of atmospheric water, as vapor, or in condensed phase as hydrometeors (liquid drops or ice particles, suspended in clouds or falling as precipitation), have gone a long way. These radiometric measurements are either made in the optical domain (visible and infrared) or in the microwave domain.

Optical imagery can operate from geostationary orbit (GEO, 36 000 km altitude). The GEO orbit allows one single instrument to cover continuously a wide section of the globe (half of it in theory); the most recent GEO optical imagers being able to perform a full-disk scan every 10 minutes. In practice, considering the geometrical distortions arising from projecting a spherical surface on a plane, a minimum of four GEO satellites is necessary to cover the whole globe (and the polar regions of the Earth are in fact not covered by GEO imagery). In contrast, in the microwave domain, physical measurement constraints impose that the remote sensing of atmospheric water is performed from a closer distance, from low Earth orbit (LEO, typically between 400 and 2 000 km altitude). Passive microwave radiometers on LEO have a scan swath width of 1700 km at most and complete between 15 and 20 orbits around the Earth every day. A minimum of about 8 passive microwave radiometers in LEO is therefore necessary to cover the whole globe every 3 hours, and more than a hundred instruments on synchronized orbits would be necessary to match the 10 min temporal sampling of GEO optical imagery.

While frequent sampling and global coverage is more easily achievable with GEO optical imagers than with LEO microwave radiometers, microwave radiometry provides more direct information than optical imagery regarding the clouds' water content and the precipitation process (as visible and infrared frequencies cannot penetrate optically thick clouds). Nowadays, the most accurate satellite global quantitative precipitation estimation (QPE) products rely essentially on LEO passive microwave measurements, GEO infrared measurements being used to "fill the gaps" between overpasses of passive microwave radiometers [Kidd et al. 2021]. A few attempts have been made to supplement passive microwave brightness temperature information with GEO infrared brightness temperature information to improve the accuracy of instantaneous estimates of precipitation intensity at the times of passive microwave overpasses [Gorooh et al. 2022]. However, it is generally found that adding only the collocated infrared brightness temperature at the time of the microwave observation leads to very little improvement as compared to using the microwave observations alone.

Yet, the ability of GEO imagery to continuously monitor the life cycle of cloud systems, from their initiation to their dissipation, is not matched by LEO microwave radiometry. The operational algorithms retrieving atmospheric hydrometeor profiles and atmospheric water content from microwave spectral signatures operate in an "instantaneous snapshot" framework, and do not exploit the temporal information in the observations. We assert here that the complementarity between GEO and LEO observations is not

fully exploited by the current operational QPE algorithms. The present study suggests new directions toward efficiently using together these different types of satellite observations to improve global QPE products.

Even when observations are available at regular time intervals and with high-frequency sampling, as is the case with the 10-min GEO imagery, exploiting temporal information and analyzing the temporal dynamics of clouds is rendered non-trivial by the clouds' motion. Indeed, as clouds can travel over thousands of kilometers, one cannot fully comprehend their life cycle by analyzing the temporal variability of the observed atmospheric signal at a fixed location (Eulerian approach). To follow the evolution of clouds over time, one must be able to track their displacements (Lagrangian approach). Over the years, various cloud-tracking algorithms have been developed to automatically detect and track clouds systems in sequences of GEO infrared satellite images [Smith and Phillips 1972, Wolf et al. 1977, Escrig et al. 2013, Ai et al. 2016, Feng et al. 2021, 2023]. In the present article we utilize the outputs of the TOOCAN cloud tracking algorithm [Fiolleau and Roca 2013-A] to analyze the life cycle of cloud systems in the tropics over South America, Africa and the Atlantic Ocean. The TOOCAN information is cross analyzed with passive and active microwave observations from the Global Precipitation Measurement (GPM) Core Observatory satellite. The first objective of our analysis is to establish a climatology of cloud systems focusing on their macro-physical characteristics, including, size, life duration, precipitation intensity, precipitation top height, convective and stratiform fractions. The cloud tracking information allows us to derive a dynamical climatology by statistically characterizing the quantities of interest and their inter-relationships at every stage of the life cycle of cloud systems. The second objective of our analysis is to assess the consistency between the estimates of precipitation intensity derived respectively from the active radar (DPR) and passive radiometer (GMI) onboard the GPM Core Observatory satellite, at the different stages of the clouds' life cycle. As part of this second objective, we analyze in particular the biases and errors in the operational NASA Goddard PROFfiling (GPROF) algorithm, which derives precipitation intensity from passive microwave spectral signatures, and which is the basis of the global satellite mapping of precipitation operated through the international GPM constellation (Hou et al. 204, Kidd et al. 2021). We eventually aim at demonstrating the potential of GEO cloud tracking information for improving global satellite precipitation mapping products, in particular their representation of the life cycle of precipitating cloud systems.

The article is organized as follows: Section 2 presents the study areas, the data and the analysis methods; Section 3 presents the results, in terms of climatology of cloud systems, and in terms of evaluation of precipitation intensity estimates derived from GPM passive microwave measurements against estimates derived from active measurements; Section 4 presents a discussion of the results and perspectives for improved global cloud and precipitation products.

2) Study regions, data, and method

2.1 Study regions: Amazonia, Central Africa, Sahel, Gulf of Guinea and Central Atlantic Ocean

Five tropical regions are selected for the analysis (see Figure 1): Amazonia (land between latitudes 8°N and 20°S and longitudes 43°W and 65°W), Central Africa (land between latitudes 8°N and 10°S and longitudes 8°E and 35°E), Sahel (land between latitudes 25°N and 8°N and longitudes 18°W and 30°E), Gulf of Guinea (ocean between latitudes 7°N and 20°S and longitudes 20°W and 14°E), and Central Atlantic Ocean (ocean between latitudes 30°N and 0° and longitudes 55°W and 15°W). Each of these regions is selected to have a spatially homogeneous climate. Amazonia and Central Africa have a tropical humid climate [Marengo and Nobre 2001, Garreaud et al. 2009, Farnsworth et al. 2011]. Sahel has a hot semi-arid climate with more than 90% of the annual precipitation amount occurring during the wet season (June to September) [Nicholson 2018, Biasutti 2019]. The selected regions of the Atlantic Ocean are both part of the tropical belt with strong influence of the intertropical convergence zone [Biasutti et al. 2004, Gu and Adler 2006]. Sea surface temperature warm pools regularly occurring in the Gulf of Guinea lead to the formation of a high number of oceanic mesoscale convective cloud systems in this region [Gu and Adler 2004].

2.2 TOOCAN tracking data, DPR and GMI data

The present study relies on the conjoint analysis of the TOOCAN cloud tracking data derived from GEO infrared imagery with estimates of precipitation type (convective or stratiform) and intensity, as well as precipitation top height, derived from active and passive microwave radiances measured by the GMI and DPR instruments onboard the GPM Core observatory satellite.

The Tracking Of Organized Convection Algorithm through a 3-D segmentatioN (TOOCAN) [Fiolleau and Roca 2013-A] detects cloud systems and tracks them over time in series of GEO infrared images produced by the imagers onboard the GOES (operated by NOAA), Meteosat (operated by EUMetSat) and Himawari (operated by JMA) satellite series. TOOCAN operates at the 30 min and 4 km resolution, which corresponds to the coarsest instrumental resolution among the different imagers it relies on. (It is however worth noting that the newest generations of GEO meteorological satellites, such as GOES-R, MTG, and Himawari-8/9, offer capabilities to perform the cloud tracking at a finer resolution of 10 min and about 1 km). For the areas and period of our study, the input images of TOOCAN come from the GOES-13 imager and the SEVIRI imager onboard Meteosat-10. The TOOCAN algorithm attributes a unique ID to each individual cloud system it detects, and defines its coverage area in each individual GEO infrared image, every 30 min. The algorithm relies on image thresholding, object detection (segmentation) and object dilation procedures, and on the computation of overlapping ratios between the objects detected in successive images [Fiolleau and Roca 2013-A].

The GPM core observatory satellite carries the active Dual-frequency Precipitation Radar (DPR) as well as the passive GPM Microwave Imager (GMI) [Hou et al. 2014]. The Combined Radar-Radiometer Algorithm (CORRA) derives precipitation intensity in three dimensions within the swath of the DPR

(which is embedded within the larger swath of GMI) with a 5 km horizontal resolution and a 250 m vertical resolution [Grecu et al 2016]. The Goddard PROFfiling algorithm (GPROF) [Randel et al. 2020, Pfreundschuh et al. 2023] provides estimates of near-surface precipitation intensity from the GMI passive radiometric measurements alone, with a 13 km by 5 km horizontal resolution. For both CORRA and GMI-GPROF, the product version 7 is used in the present study. While the DPR has a swath width of 250 km and is currently the only scanning precipitation radar in space whose data is made available to the research community, GMI has a swath width of 885 km, and moreover, several other passive microwave imagers similar to GMI, such has AMSR-2 and the SSMI/S series, orbit the Earth. Consequently, at any point of the Earth, passive microwave measurements are more than ten times more frequent than active measurements from the DPR, hence the interest in providing as accurate as possible quantitative precipitation estimates from passive microwave measurements alone. The less frequent active radar reflectivity measurements provide direct observation of the 3D structure of clouds and precipitation, allowing accurate estimation of the hydrometeor content of the atmosphere, and ultimately of the precipitation rate at the surface. The CORRA estimates therefore serve as a global reference for the calibration and training of passive microwave precipitation retrieval algorithms. The GPROF algorithm in particular relies on an a-priori database made of a large set of passive microwave spectral signatures associated with coincident estimates of surface precipitation intensity from the CORRA algorithm. GPROF is thus designed to reproduce CORRA estimates as accurately as possible. For this reason, in the present study, the CORRA precipitation estimates are considered as the reference for the evaluation of GPROF. In addition to estimates of precipitation intensity we also utilize estimates of precipitation type (i.e. stratiform or convective precipitation) and of precipitation top height derived from the DPR, to assess the dependance of GPROF's retrieval accuracy on these quantities.

It is worth noting that, in the present study, we use "level-2" GPM estimation products, which rely on direct radiometric observations, without interpolation or dynamical physical simulations involved [NASA 2021]. The level-2 estimation products are sparse in the sense that they are orbit-based and only provide estimations at the locations and times of the satellite overpasses. Other studies have performed similar analyses relying on higher-level products [e.g., Roca et al. 2014, Berthet et al. 2017, Roca and Fiolleau 2020, Cui et al. 2020, Feng et al. 2021], such as the IMERG multisatellite QPE product, which provide precipitation estimates projected on a regular spatiotemporal grid, by dynamically integrating radiometric measurements from several satellite platforms, referred as level-3 and level-4 products [NASA 2021]. While level-3 and level-4 gridded products can potentially provide a much larger sample size, they are subject to larger state-dependent biases and inaccuracies than level-2 products, the interpolation and data-merging procedures leading to level-3 and level-4 products are also prone to alter the temporal dynamics of the precipitation signal [Guilloteau et al. 2021, 2022, Li et al. 2023].

2.3 Data collocation

In each one of the five study regions, for each GPM overpass over the 2015-2016 study period, GMI-GPROF precipitation estimates falling within the swath of the DPR are collocated with CORRA

estimates and mapped on the CORRA 5-km grid using a simple nearest-neighbor interpolation. Each CORRA pixel and its corresponding re-mapped GPROF pixel are then associated to the closest TOOCAN system (if any within a 4 km radius). Because the DPR and GMI are onboard the same platform, their coincident observations are only a few seconds apart. Given the 30-minute temporal sampling of the TOOCAN product, the maximum temporal delay between any DPR measurement and its collocated TOOCAN cloud system is 15 minutes. Figure 2 shows an illustrative example of a cloud system tracked by TOOCAN over southwestern Brazil for 12.5 hours (from 2015-11-13 14:00 UTC to 2015-11-14 02:30 UTC), and sampled once by GPM, on 2015-11-13 at 19:30 UTC.

Over the three land areas, Amazonia, Central Africa and Sahel, respectively, 110 000, 115 000 and 48 000 unique systems have been tracked by the TOOCAN algorithm for the 2015-2016 period. Regarding the oceanic regions, 88 000 cloud systems have been tracked over the Central Atlantic Ocean and 47 000 over the Gulf of Guinea. Because of the sparsity of GPM direct observations, only a fraction of these systems has been sampled by both GMI and the DPR. However, the two-year length of the analysis period and the size of the chosen study areas (all five areas greater than 4 million km^2) ensure that, in each region, the number of unique systems sampled is of several thousands (9500, 9900, 5100, 8000 and 4500 over Amazonia, Central Africa, Sahel, Central Atlantic Ocean and Gulf of Guinea respectively). Because individual cloud systems are rarely sampled by GPM more than once during their lifetime, all the statistics describing the evolution of GPM-observed quantities during the life cycle of cloud systems in the present study are computed as composites over thousands of cloud systems.

2.4 System's life stage

For each TOOCAN system that could be tracked continuously from its initiation to its dissipation, we segment its life cycle into five equal-duration development stages. The development stage at time *t* is defined as:

$$S(t) = ceil(5 \times \frac{t-t_i}{D})$$

$$\text{with: } D = t_d - t_i$$

where $ceil(.)$ designates the "ceiling" function which, to a real *x*, associates the smaller integer I_x such as $I_x > x$; t_i designates the initiation time of the system and t_d its dissipation time, *D* therefore being the total life duration of the system. For our study, the five-stage segmentation is applied to all systems with $3\ h < D < 48\ h$. Systems with a life duration less than 3 hours are excluded because of the limiting 30-min temporal resolution of TOOCAN. In our analysis, systems are separated into three duration categories: short-lived systems (3 to 6 hours), medium-lived systems (6 to 12 hours), and long-lived systems (12 to 48 hours). The 48-hour upper duration limit for long-lived systems excludes hurricanes, for which we assessed that two years of GPM observations were insufficient to accurately resolve the average life cycle. Because of the relative rarity of hurricanes, combined with DPR's narrow swath and its several-day revisit time, only a few dozens of DPR overpasses per year over hurricanes are available for analysis.

It is important to note that the initiation and dissipation times of each system are defined only from the outputs of TOOCAN. The TOOCAN algorithm is designed for tracking the trajectory of organized cloud systems rather than for detecting areas of initiating convection. The very early stages of the development of clouds, before they meet the conditions for being identified as an organized system by TOOCAN, are therefore not accounted for in this study, although precipitation may occur during this earlier phase. Detecting and tracking clouds at their earliest development stages, when they are still scattered and not yet organized as compact objects, would likely require a different method than TOOCAN.
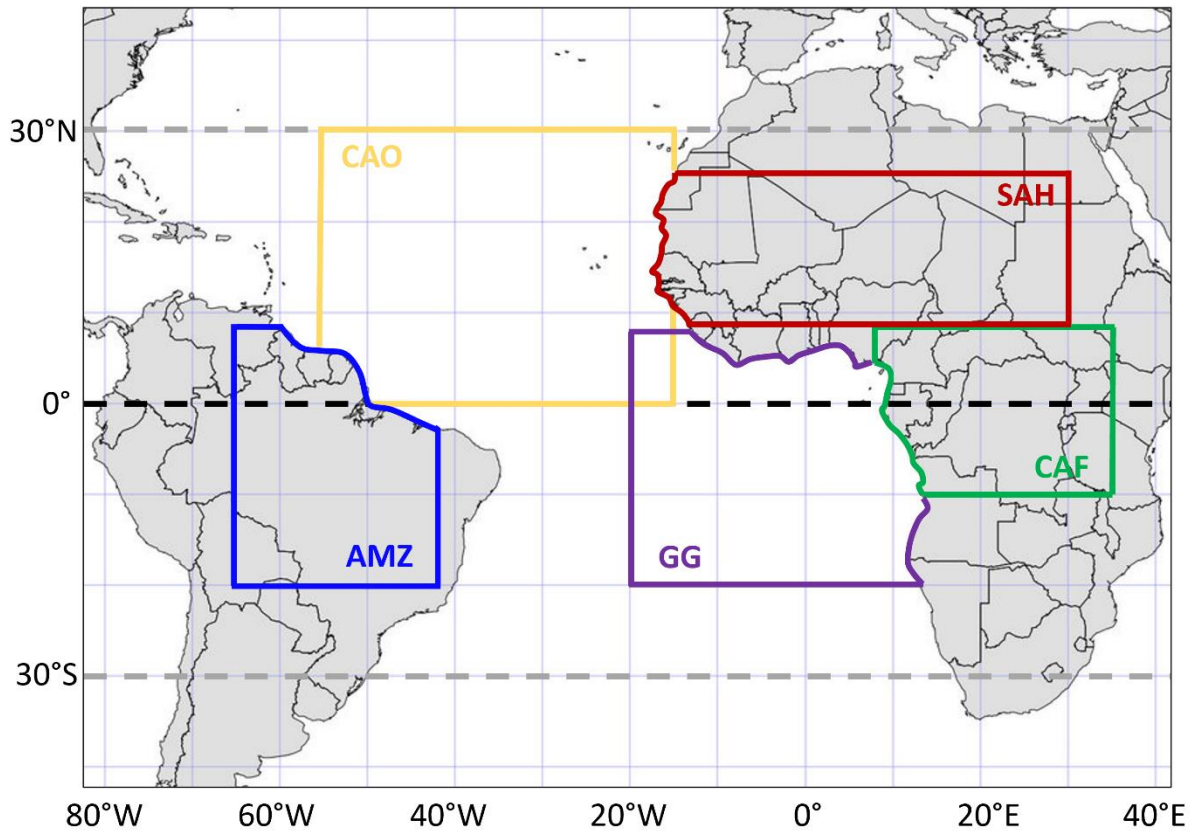
Figure 1: Map of the five tropical areas retained for the study, which are, Amazonia (AMZ), Central Africa (CAF), Sahel (SAH), Gulf of Guinea (GG) and Central Atlantic Ocean (CAO). In those regions, respectively, 110 000, 115 000, 48 000, 47 000, 88 000 unique systems have been tracked by the TOOCAN algorithm for the 2015-2016 period, out of which, 9500, 9900, 5100, 4500 and 8000 respectively have been sampled by both the GMI and DPR instruments.
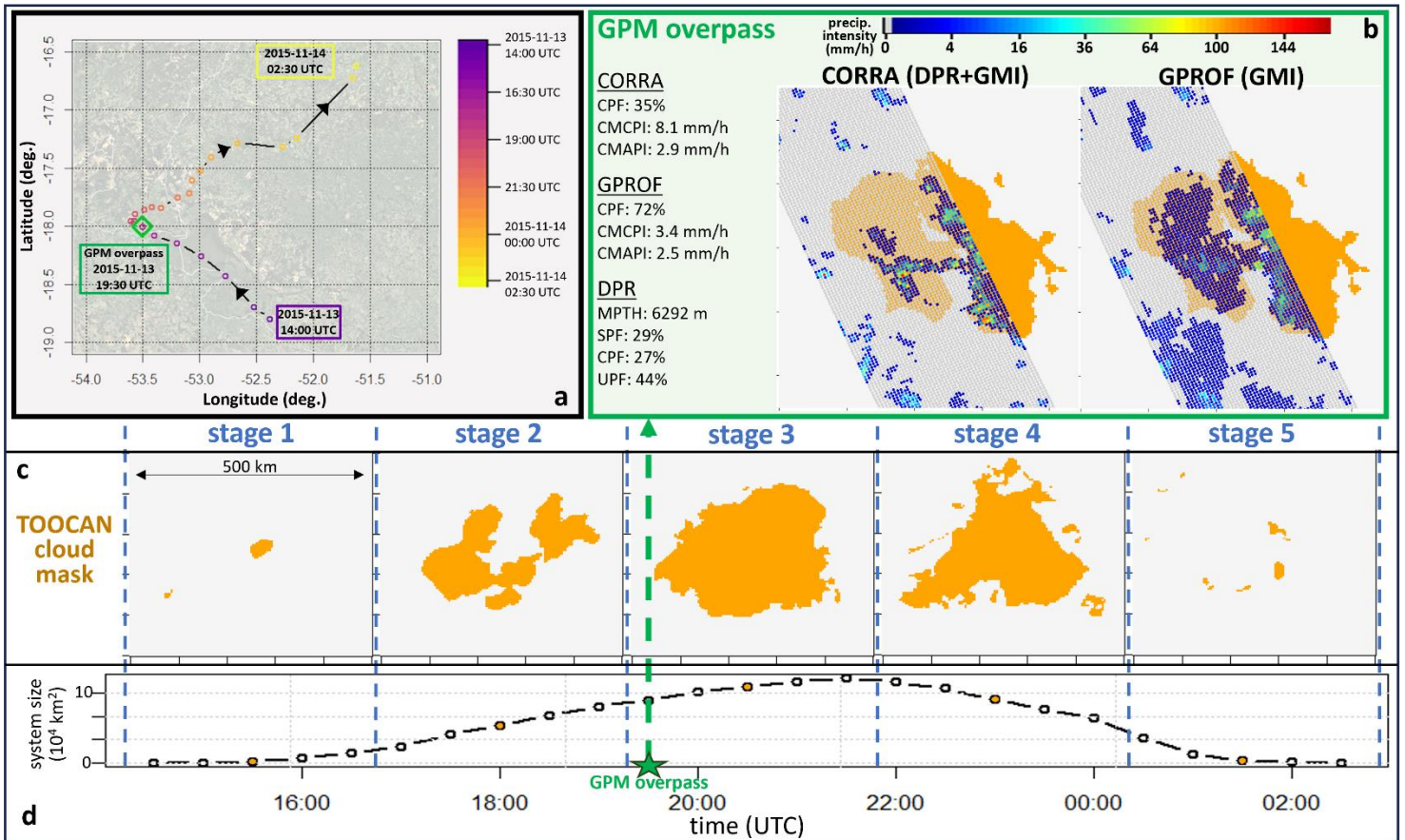
Figure 2: Illustration a of cloud system tracked by TOOCAN over southwestern Brazil from 2015-11-13 14:00 UTC to 2015-11-14 02:30 UTC, and sampled by GPM on 2015-11-13 at 19:30 UTC. The ID number attributed to this system by TOOCAN is 12895354. (a) Track of the system's barycenter derived from TOOCAN. (b) Precipitation fields from the CORRA and GPROF algorithms at the time of the GPM overpass. The precipitation statistics computed at the time of the GPM overpass are: cloud precipitation fraction (CPF), cloud mean conditional precipitation intensity (CMCPI), cloud mean areal precipitation intensity (CMAPI), mean precipitation top height (MPTH) relative to the freezing level, stratiform precipitation fraction (SPF), convective precipitation fraction (CPF) and undetermined type precipitation fraction (UPF). (c) Samples of the TOOCAN cloud mask at the five stages of the cloud life cycle. While TOOCAN's temporal sampling is 30 minutes, only one sample per stage is shown here. (d) Size of the cloud system derived from TOOCAN as a function of time. As individual cloud systems are rarely sampled by GPM more than once during their lifetime, the evolution of the different statistics during the life cycle of cloud systems (figures 4, 5, 6, 7, 8, 10, 11) are computed as composites over thousands of cloud systems.

3) Results

3.1 Climatology of cloud's morphology and dynamics from GEO tracking

In this section, only the outputs of the TOOCAN tracking algorithm are considered, to extract statistics regarding the life duration of cloud systems and the variation of cloud system's size (i.e. their horizontal extent) during the different stages of cloud's life cycle.

Figure 3 shows the frequency distribution of TOOCAN cloud systems' duration in the five regions of interest. To compute these distributions, for each climatic region, the life duration of every system that passed through is computed. This means in particular that systems that moved from one region to another, (e.g. systems that initiated over the Sahel and moved over the Central Atlantic Ocean) are included in the statistical distribution for both regions. For these systems that entered or exited a given region through their lifetime, the life duration is still computed from initiation to dissipation. The computed life duration of a given system therefore potentially includes the amount of time the system lived outside of the climatic region of interest. The distributions of systems' duration are very similar across Amazonia, Central Africa and Sahel with, respectively, 58%, 55% and 56% of the systems lasting less than 6 hours, and, 7%, 8% and 9% lasting more than 12 hours. The distributions of system duration are quasi-identical between the two oceanic areas, with 53% of systems lasting less than 6 hours and 10% lasting more than 12 hours.

Figure 4 shows the distribution of TOOCAN cloud system's size as a function of the life stage for short-lived (3 to 6 hours), medium-lived (6 to 12 hours) and long-lived (12 to 48 hours) systems, in each one of the five tropical areas. The most striking element is the symmetry in the temporal evolution of the size of cloud systems. In all areas and for all system durations the mean system size reaches its maximum during the stage 3 (middle stage) of the life cycle. These results are consistent with those of Roca et al. (2017), whose analysis also relied on the outputs of the TOOCAN algorithm. Our analysis shows that the average temporal dynamics of cloud systems is extremely consistent across all areas, including between land and ocean, and across systems' duration. The most noticeable difference across the regions is that, at every stage of the cloud life cycle, the mean system size is greater over land than over ocean, and greater over Sahel than over Central Africa and Amazonia.
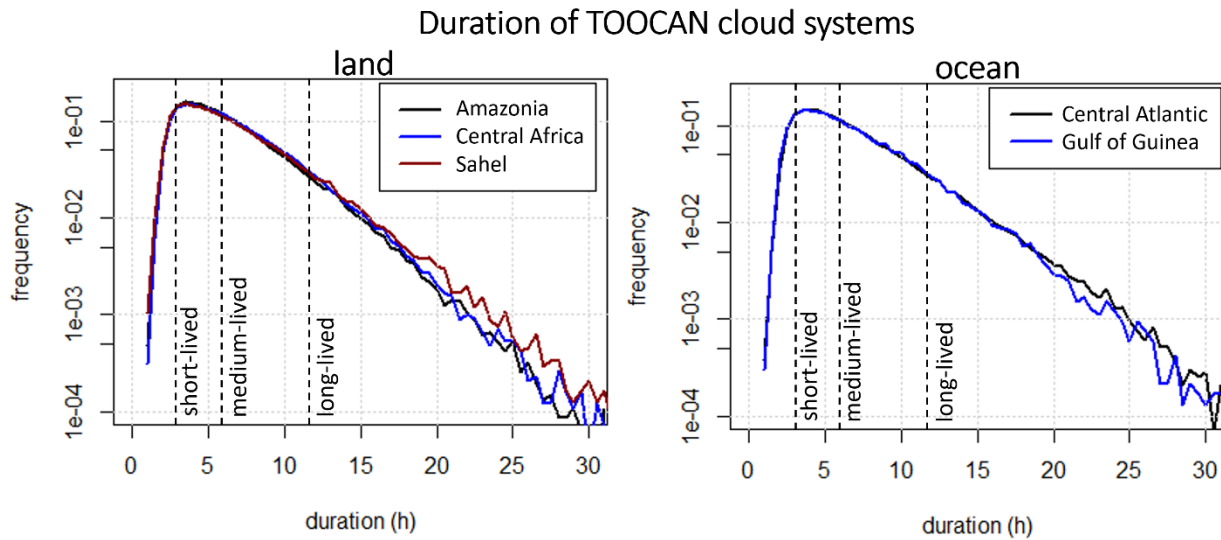
Figure 3: Frequency distribution of the duration of the TOOCAN cloud systems for each one of the five tropical areas. The percentage of short-/medium-/long- lived systems is 58%/35%/7% over Amazonia, 55%/37%/8%, over Central Africa, 56%/35%/9% over Sahel, and 53%/37%/10% over both Gulf of Guinea and Central Atlantic Ocean.
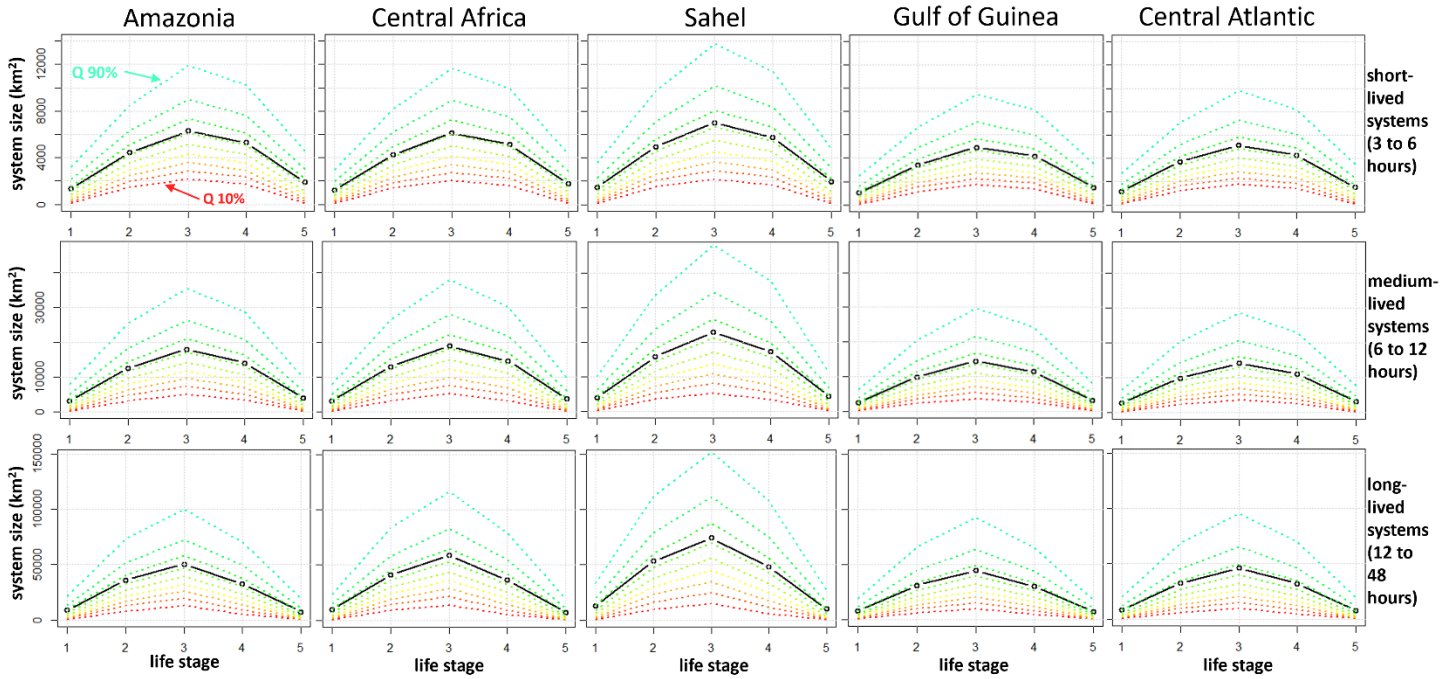
Size of cloud systems

Figure 4: Distribution of TOOCAN cloud system's size as a function of the life stage for short-lived (3 to 6 hours), medium-lived (6 to 12 hours) and long-lived (12 to 48 hours systems), in each one of the five tropical areas. The thick black line indicates the mean of the distribution, the colored dashed lines indicate the 10 to 90 percentiles (every 10 percentile).

3.2 Precipitation and vertical structure of clouds from GPM observations as a function of cloud's life stage

In this section, observations from the GPM Core Observatory satellite, collocated with the TOOCAN data are analyzed. Figure 5 shows the average precipitating fraction within the TOOCAN-delimited cloud area as a function of the cloud life stage, according to CORRA and GMI-GPROF. The precipitating fraction is defined as the fraction of pixels (at the 5-km native resolution of CORRA) with precipitation intensity above 0.2 mm/h. One can immediately notice that the precipitating fraction in GPROF is always higher than that in CORRA, especially over the Amazon and Central Africa regions. As a Bayesian algorithm, GPROF tends to artificially generate a large number of pixels with very low precipitation intensity. Indeed, because the inversion of passive microwave radiances into precipitation intensity is an underconstrained problem, the GPROF estimation is probabilistic: the estimated value given by GPROF is the mean of the a-posteriori probabilistic distribution of precipitation intensity given the observed radiances. In the frequent cases when the a-posteriori distribution contains both zero and non-zero values, those are averaged together, inducing a low value of the estimated intensity. This is the reason why a 0.2 mm/h threshold is used here to define precipitating fraction instead of counting all pixels above 0.0 mm/h. Indeed, with a 0.0 mm/h threshold, the cloud precipitating fraction in GPROF is found nearly constant at 100%. Beyond the fact that GPROF mean precipitating fraction at 0.2 mm/h is always higher than that of CORRA, one can see that the two estimates are consistent with each other in terms of the temporal evolution of the mean precipitating fraction during the life cycle of cloud systems. For short-lived systems, in all the studied regions, the precipitating fraction decreases monotonically as the systems mature. For long-lived systems the precipitating fraction is relatively constant during the first half of the life cycle and decreases during the second half. It must be noted that the average cloud precipitating fraction is lower and varies less in the Sahelian region as compared to the other regions.

Besides the temporal evolution of the cloud precipitating fraction, we are interested in the evolution of precipitation intensity during clouds' life cycle. Figure 6 shows the mean conditional precipitation intensity, which is computed as the mean intensity for pixels above 0.2 mm/h, as a function of clouds' life stage. The counterpart of the systematically higher precipitating fraction in GPROF is a systematically higher conditional intensity in CORRA. This can be seen as a compensation mechanism, as GPROF estimates are designed to preserve the mean value of CORRA. It must be noted that, in Bayesian minimum mean square error estimation methods, the mean is the only moment of the statistical distribution of the target variable that is strictly preserved in theory. Additionally, the statistical distribution of the estimates is generally biased toward the mean, leading to compressed dynamical range, reduced statistical variance, and underrepresentation of the extremes on both sides of the distributions [Guilloteau et al. 2023]. We note that, from a statistical point of view, for precipitation rates, zero is an extreme value, as it is the absolute minimal possible value (even if zeros are very frequent). This explains why the statistical distribution of precipitation rates in GPROF is so different from that of CORRA. GPROF estimates are always "smoother", with a higher number of low-intensity pixels and lower high extreme values than CORRA. Another element contributing to the differences between GMI-GPROF and CORRA in terms of statistical distribution of precipitation rates is their different native resolution, and, in a more

extensive way, their different "effective resolution". As mentioned in the data collocation section (2.3) the nominal resolution of GMI-GPROF estimates is 13 km by 5 km. For this study, GPROF estimates are interpolated on the 5 km by 5 km grid of CORRA using a nearest neighbor interpolation (which preserves the statistical distribution of the interpolated variable). Because GPROF uses information from different microwave channels with different footprint sizes, its actual resolution is not trivial to define. Published studies have shown that over land, GMI-GPROF can only resolve precipitation features at scales down to about 40 km at best [Guilloteau et al. 2017, Pfreundschuh et al. 2023], we therefore stipulate that the "effective resolution" of GMI-GPROF over land is approximately 40 km.

Despite their differences, GPROF and CORRA both show the mean conditional precipitation intensity generally decreasing monotonically as systems mature over both ocean and land (Figure 6). We can however notice that for long-lived systems over oceans the mean conditional precipitation intensity remains quasi constant from stage 1 to stage 2. Figure 7 shows the evolution of the mean areal cloud precipitation intensity, which is computed over all pixels, including non-precipitating pixels. In contrast to what is shown in Figure 4 for the cloud horizontal extent, what is striking in the figures 5, 6 and 7 for the precipitation occurrence and precipitation intensity is the temporal asymmetry, with precipitation occurrence and intensity generally decreasing with aging cloud systems. For short-lived systems the curves of cloud mean areal precipitation intensity against time (Figure 7) are rather convex, with a stronger decrease rate at the beginning of the event. In contrast, the curves are rather concave for long-lived events with a weak decrease rate at the beginning. For medium-lived events the curve is more linear with a nearly constant decrease rate.

As expected, the differences between GPROF and CORRA in terms of precipitating fraction and conditional intensity tend to compensate each other; significant stage-dependent biases however persist over land (Figure 7). Over the two oceanic areas, GPROF and CORRA estimates of the cloud mean areal precipitation intensity as a function of cloud's life stage are highly consistent, both in terms of absolute magnitude and in terms of dynamics (shape of the curve). Over Amazonia, Central Africa and Sahel, GPROF is found to significantly underestimate precipitation intensity as compared to CORRA at the stages 1 and 2 of the life cycle, for all short-, medium- and long-lived systems. This underestimation pattern is remarkably consistent across the three land regions and the different system life durations. Altogether GPROF overestimates the mean precipitation intensity inside TOOCAN-identified-systems' areas by about 4% over the two oceanic regions, and underestimates it by about 16% over the three land regions. From Figure 7 we also notice that the standard deviation of the GPROF error (grey dashed line), computed as the standard deviation of the pixel-wise differences between GPROF and CORRA at the 5-km resolution, is higher at the early stages of cloud life cycle, when the mean precipitation intensity is the highest.

Figure 8 also shows the comparison between GPROF and CORRA during the five stages of clouds' life cycle, but in terms of the distribution of the total rain volume instead of precipitation intensity, i.e. taking into account both the mean areal intensity and the system's size. One can see that the stage-

dependent intensity biases of GPROF over land induce a shift of the center of mass of the precipitation volume toward the later stages of the cloud life cycle as compared to the distribution derived from CORRA. For medium- and long-lived systems over land, while the intensity is the highest and the intensity bias is the strongest at the stage 1 (Figure 7), this stage only moderately contributes to the total precipitation volume and to the volume bias (because of the relatively small size of the systems at this stage, as shown in Figure 4). One shall note however that, even if they only marginally contribute to the global precipitation amount, high intensity precipitation rates concentrated over small areas can result in extreme impacts (e.g. flash floods and landslides); hence the importance of accurately retrieving them, and properly identifying their associated retrieval biases if any.

Figure 9 shows the cumulative fractional contribution of systems of increasing life duration to the total rainfall amount in the different regions, as estimated from the CORRA and GPROF products, collocated with the TOOCAN information. In each region, the curve derived from the CORRA data nearly perfectly matches the curve derived from the GPROF data; the curves are in fact barely visually distinguishable on the figure. This demonstrates that the life-stage-dependent biases of GPROF do not induce a duration-dependent bias, i.e., that the relative bias of GPROF against CORRA, when integrated over the whole life cycle, is identical for all system durations. The cumulative distributions shown in Figure 9 reveal the importance of long-lived systems (above 12-hour duration), which, while they account for only 7 to 10% of all systems, contribute to 50 to 60% of the precipitation amount over the land regions and around 70% over the oceanic regions. We shall here give attention to the fact that only the CORRA and GPROF pixels that could be associated to a TOOCAN system are accounted for in this study (see section 2.3). Precipitating pixels that are not within 4 km of a TOOCAN system account for 25% and 32% of the total precipitation volume in CORRA and GPROF respectively over the analyzed areas and period. Part of this unaccounted precipitation comes from precipitating systems other than the MCSs tracked by TOOCAN. Part of it may be due to precipitation occurring before the start of TOOCAN's tracking. It appears from our analysis that, when TOOCAN starts tracking a cloud system, most of the time, it has already entered a precipitating phase.

To better understand the temporal patterns of the bias of GPROF against CORRA and try to relate them to cloud's physical properties, we analyze the evolution of precipitation top altitude relatively to the altitude of the freezing level (Figure 10) and precipitation type (Figure 11) along the life cycle of the clouds. Precipitation top height is found to generally decrease from stage 2 to stage 5. During the first two stages, the average precipitation top height is relatively constant; this contrasts with the mean precipitation intensity (Figure 7), which was found to significantly decrease from stage 1 to stage 2, particularly for short-lived systems. From the quantile curves in Figure 10 we can also see that the dispersion in the statistical distribution of precipitation top height decreases as the system matures, revealing a stronger variability of the vertical structure of precipitation across different systems (and within systems) at the earlier stages of clouds' life cycle. This higher variability of precipitation top height at the early stages coincides with higher standard deviation of the error (against the CORRA reference) in GPROF estimates of precipitation intensity (Figure 7, grey dashed curves). Figure 11 shows that the average convective

fraction of clouds significantly decreases from stage 1 to stage 3. In short-lived systems, the decrease of the convective fraction over time coincides with increasing rate of "undetermined" precipitation type, i.e. DPR reflectivity profiles that could not unambiguously be labeled as convective or stratiform by the classifier algorithm. In long-lived systems the rate of undetermined precipitation type is relatively constant and the decrease of the convective fraction over time coincides with increasing stratiform fraction. It is worth noting that, over the land regions, the magnitude of both the systematic bias and the random errors (Figure 7) of GPROF against CORRA scale positively with the convective fraction but seem to be relatively unaffected by the rate of "undetermined" reflectivity profiles.

The general pattern of GPROF's biases over land as a function of clouds' life stage is consistent with the already-known pattern of systematic underestimation of high-intensity convective precipitation [Henderson et al. 2017, Petković et al. 2019, Pfreundschuh et al. 2023]. This intensity-dependent bias can again be partially attributed to the Bayesian minimum mean squared error estimation process of GPROF, which, by design, produces smooth estimates with compressed dynamical range and reduced temporal variability. The excessively smooth dynamics of GPROF over land indicates that the algorithm has difficulty differentiating clouds in their growing phase, with intense active convection and high precipitation intensity, from more mature clouds, with less intense or decaying convection. Over land, as the emission signal by liquid raindrops is hardly distinguishable from the background surface emission signal in the microwave domain, the GPROF algorithm essentially exploits the signal resulting from the scattering effect of ice particles in the upper levels of the clouds. While the ice scattering signal is certainly a strong indicator of atmospheric convection, the maximum intensity of the ice scattering is likely delayed in time as compared to the maximum of convective activity. Indeed, when convection is active, ice particles are expected to progressively accumulate in the upper cloud levels. Later, in the dissipating phases of the clouds' life cycle, even if the convective activity decreases rapidly, the ice particles may remain suspended in the upper cloud levels for several tens of minutes and up to a few hours. Supplementing the inputs of the GPROF algorithm with information on the temporal dynamics of clouds could therefore help improve the estimation of the instantaneous precipitation intensity.
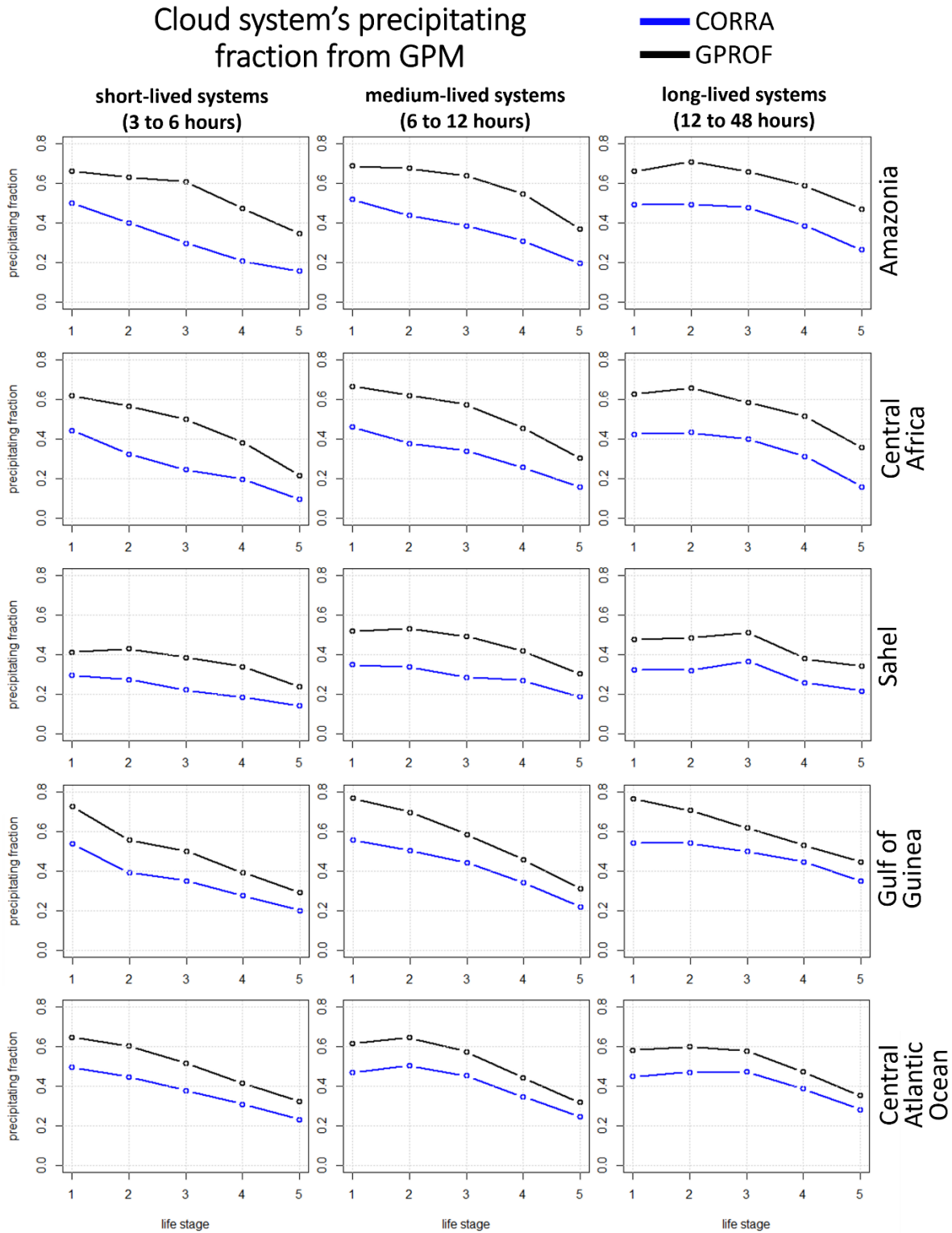
Figure 5: Mean cloud precipitating fraction as a function of TOOCAN cloud system's life stage according to the CORRA (blue line) and GMI-GPROF (black line) estimates. The precipitating fraction is defined as the fraction of the cloud area with precipitation intensity above 0.2 mm/h.
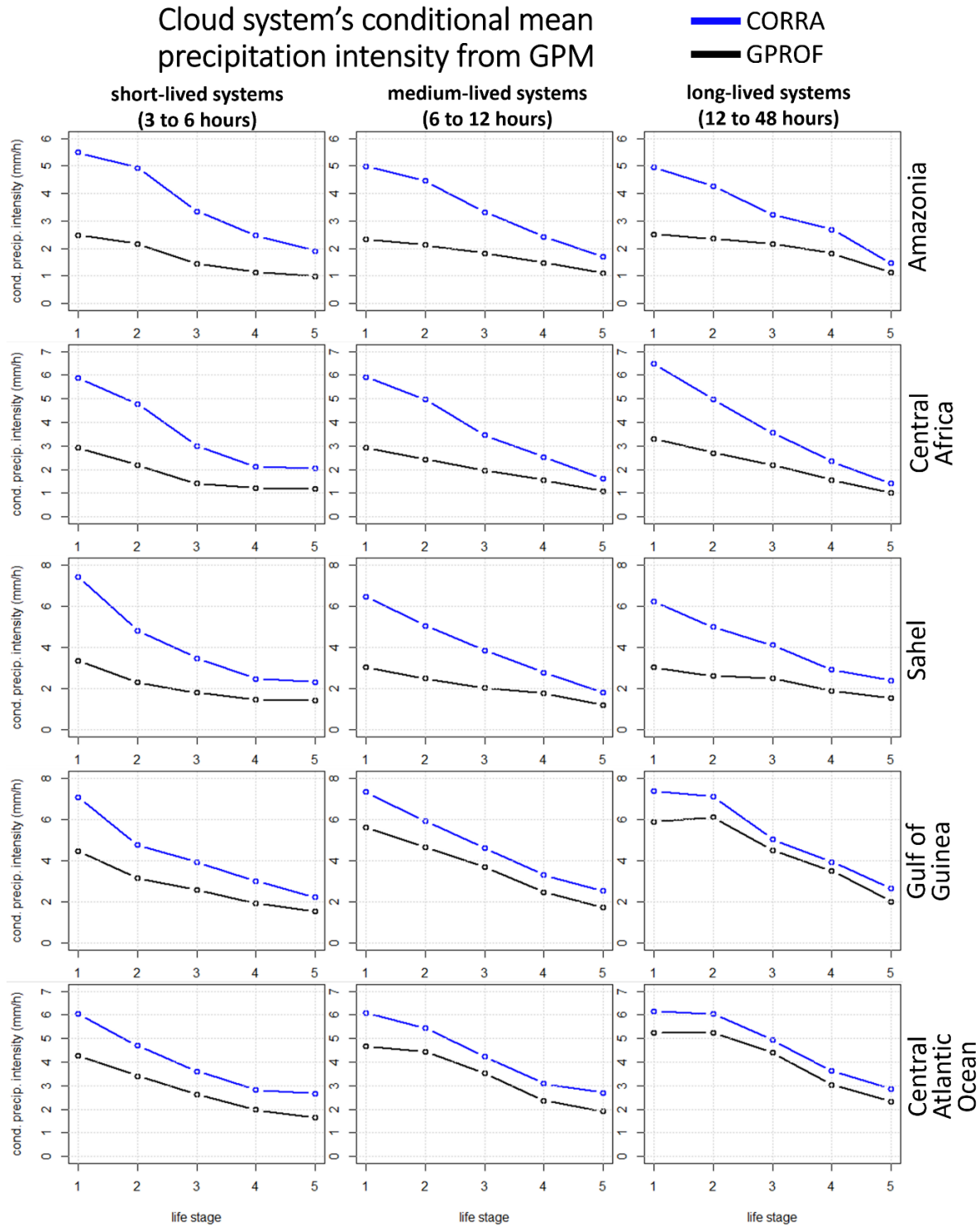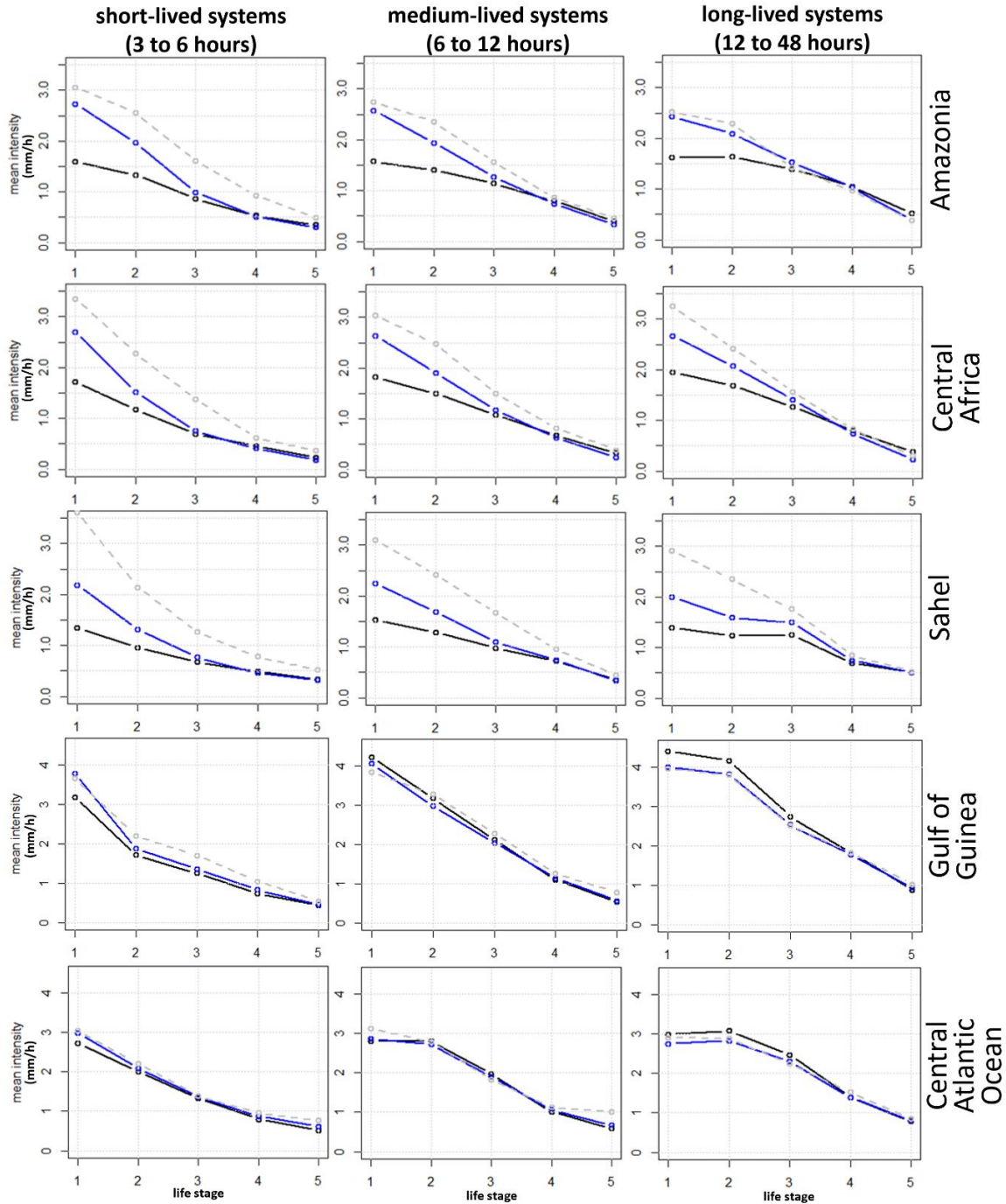
Figure 6: Mean conditional precipitation intensity as a function of TOOCAN cloud system's life stage according to the CORRA (blue line) and GMI-GPROF (black line) estimates. The conditional mean precipitation intensity is defined as the mean intensity computed over precipitating pixels only (i.e. pixels with intensity above 0.2 mm/h).

Figure 7: Mean areal precipitation intensity as a function of TOOCAN cloud system's life stage according to the CORRA (blue line) and GMI-GPROF (black line) estimates. The grey dashed line shows the standard deviation of the difference GPROF-CORRA as a function of cloud system's life stage.
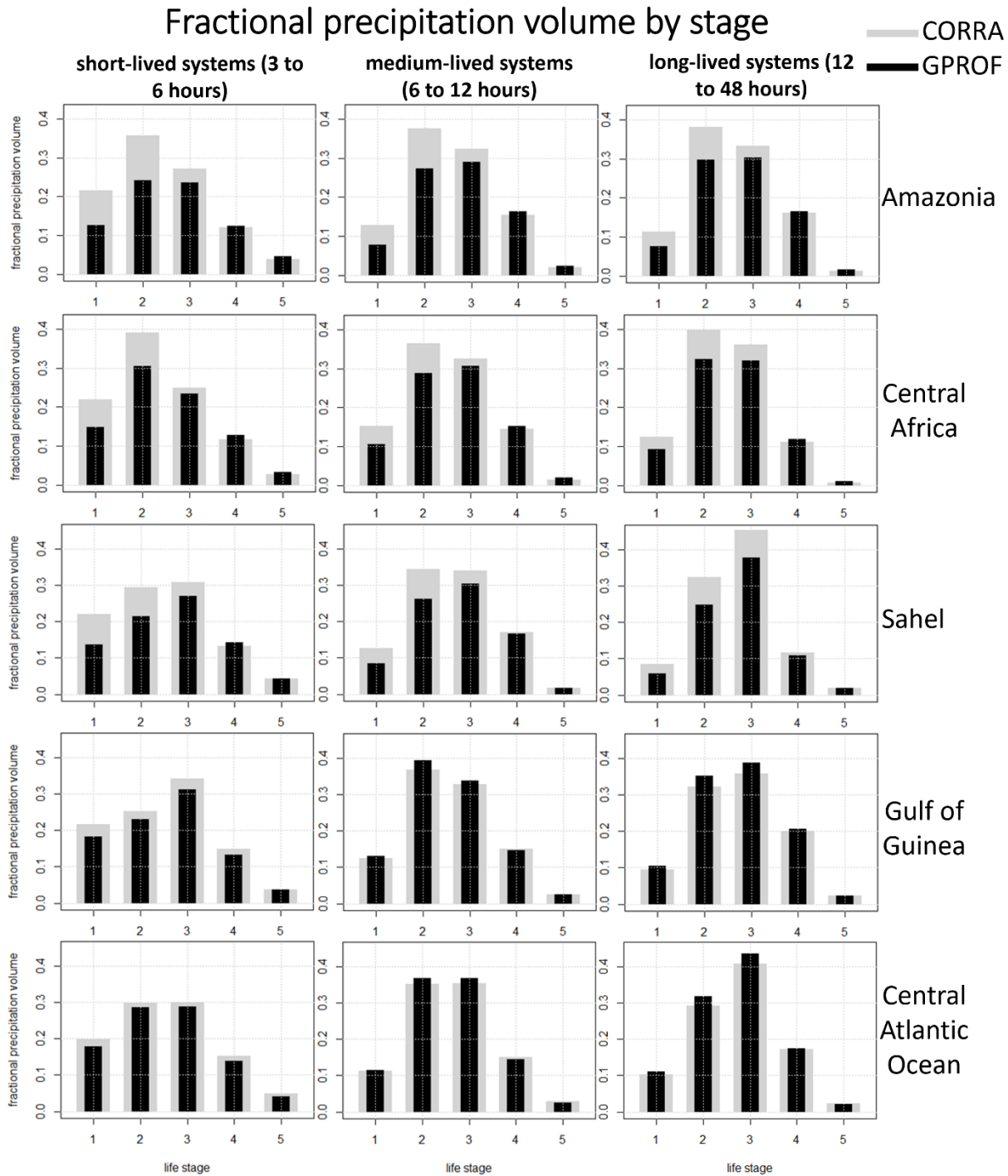
Figure 8: Contribution to the total rainfall volume of the five life stages according to the CORRA (grey) and GMI-GPROF (black) estimates. For each life stage, the fractional contribution is computed relatively to the total CORRA rainfall volume across all stages. Stage-dependent intensity biases of GPROF over land induce a shift of the center of mass of the precipitation volume toward the later stages of the cloud life cycle as compared to the distribution derived from CORRA.
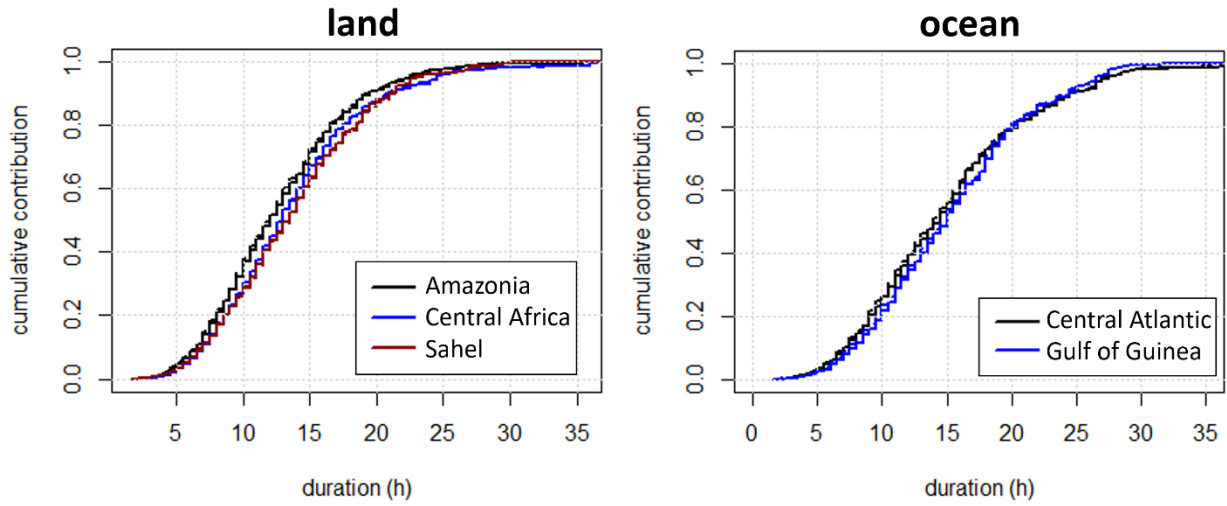
Figure 9: Cumulative contribution to the total rainfall volume as a function of cloud systems' duration. The solid lines are derived from the CORRA precipitation estimates collocated with the TOOCAN data. The dashed lines are derived from the GMI-GPROF precipitation estimates collocated with the TOOCAN data. The dashed and solid lines are nearly indistinguishable because they are on top of each other, showing the high consistency between CORRA and GPROF when it comes to the relationship between precipitation volume and system duration.
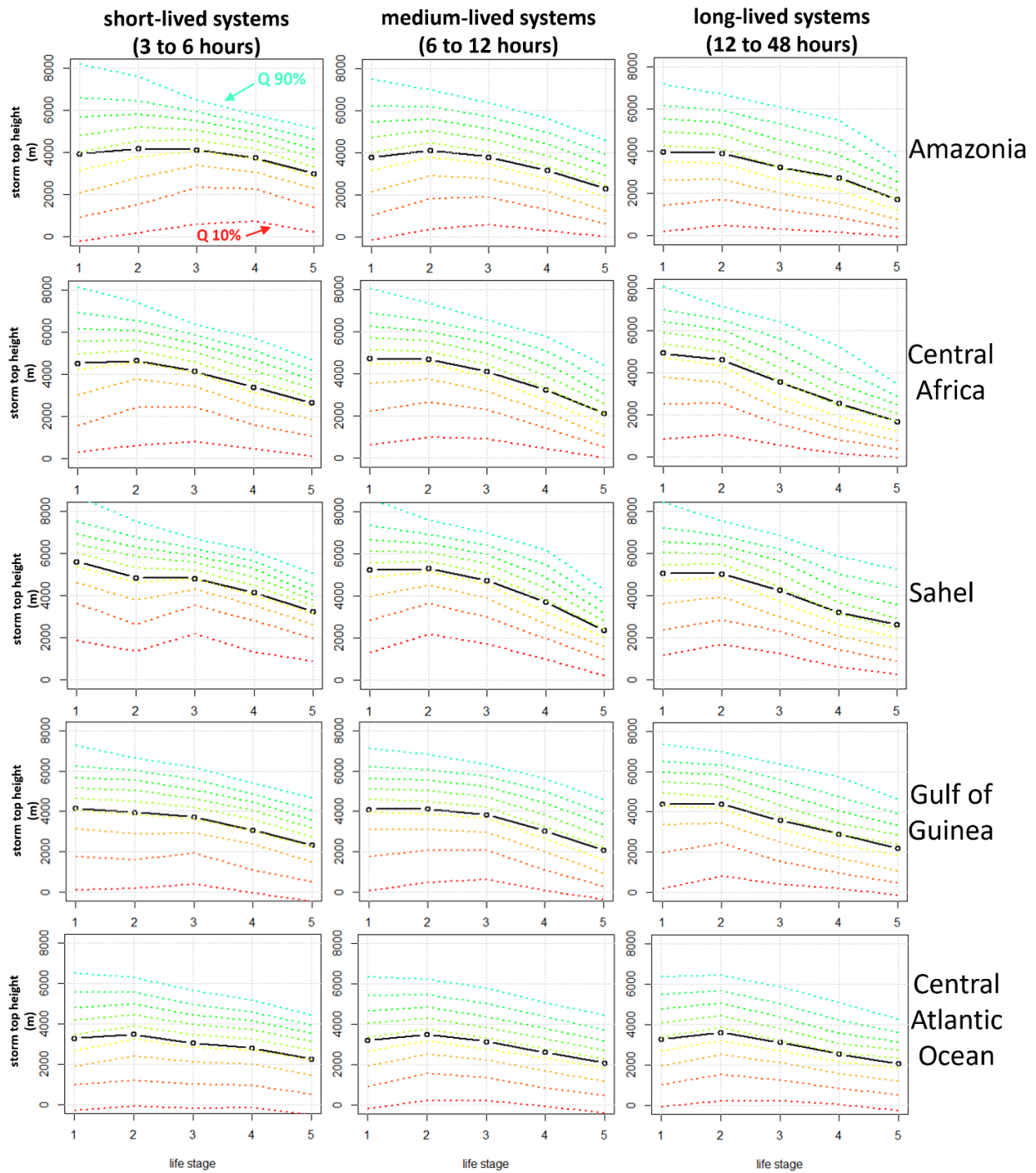
Precipitation top height

Figure 10: Distribution of GPM DPR precipitation top height relative to the altitude of the freezing level (0°C isotherm) as a function of TOOCAN cloud system's life stage. The thick black line indicates the mean of the distribution, the colored dashed lines indicate the 10 to 90 percentiles (every 10 percentile).
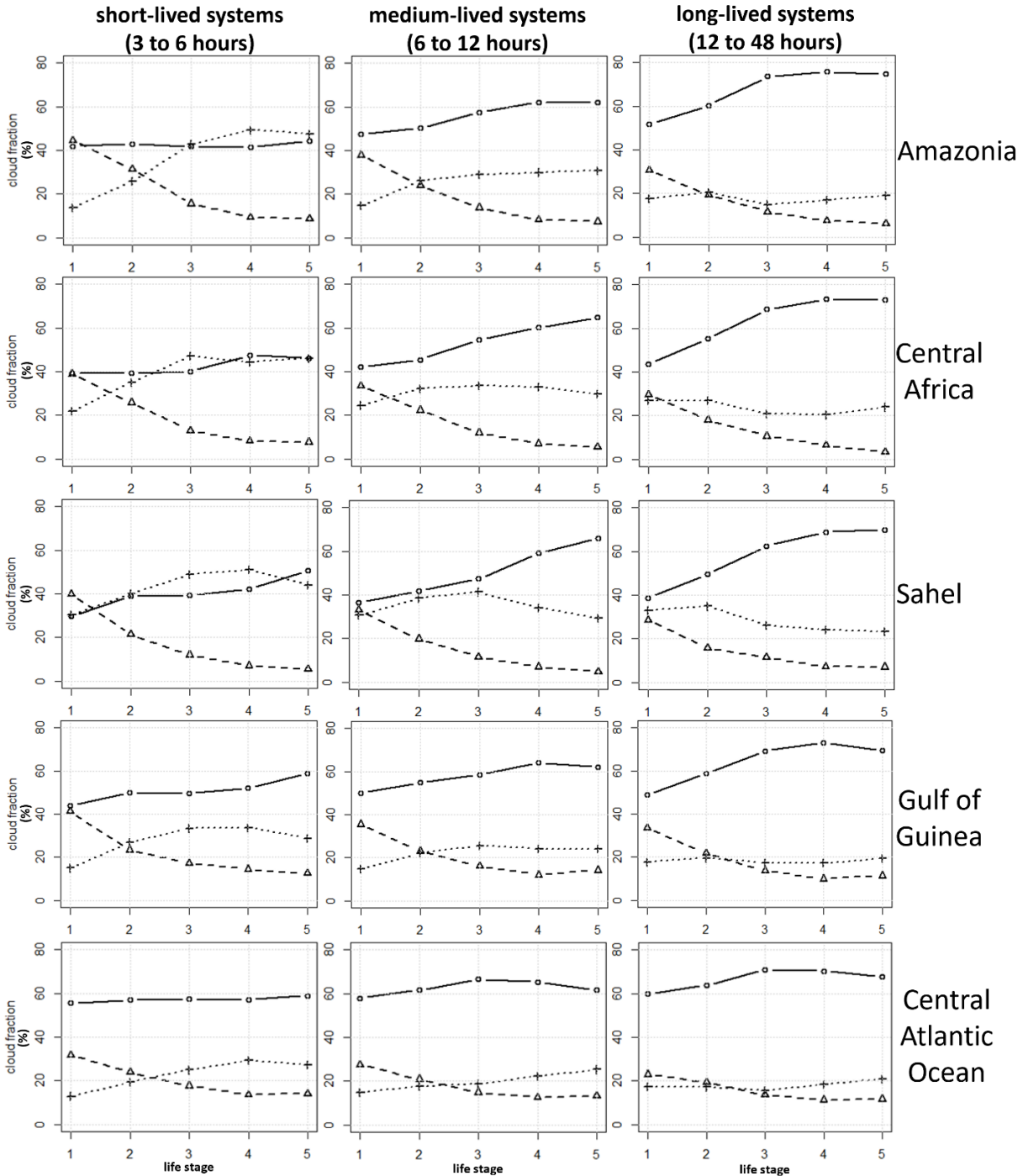
Figure 11: Stratiform, convective and undetermined type precipitation fractions as a function of cloud system's life stage according to the DPR precipitation type classification. The precipitation type fractions are computed as fractions of precipitating pixels within the cloud systems (non-precipitating pixels are not accounted for in the computation of the fractions).

4) Discussion, conclusion, and perspectives

4.1 Climatology of cloud systems

The collocation of GPM active and passive microwave measurements with the TOOCAN data allowed us to statistically characterize several properties of cloud systems at different stages of their life, including size, precipitation intensity, precipitation type and precipitation top height. The average temporal evolution of systems' properties is remarkably homogeneous across the different analyzed regions and across systems of different life duration.

The most salient aspect of the temporal evolution of the horizontal size of cloud systems is its time symmetry. On average, systems peak in size halfway through their lifetime. On the contrary, precipitation-related characteristics are strongly asymmetrical, the average convective fraction and precipitation intensity decrease continuously as systems mature. The average precipitation top height is relatively constant in the first third of the clouds' life cycle and decreases continuously in the second and third thirds of the life cycle. In addition to being highly consistent across different climatical regions and across systems of different life duration, the statistics presented here are consistent with those of previous regional or pan-tropical studies [Fiolleau and Roca 2013-B, Bouniol et al. 2016, Roca et al 2017, Elsaesser et al. 2022], which tend to indicate that the general features of the life cycle of tropical mesoscale convective systems are relatively universal.

4.2 Systematic underestimation of precipitation intensity in GMI passive microwave retrievals in the early stages of clouds' life cycle

The most salient and consistent result of the study in terms of comparison of the passive GMI-GPROF estimates of near surface precipitation rate against the active-passive CORRA estimates is the strong systematic underestimation of the mean precipitation intensity in the early stages of the cloud's life cycle (stages 1 and 2) over lands in the tropics (Amazonia, Central Africa and Sahel), independently of the total life duration of the system (between 3 and 48 hours). We note that the early stages of the life cycle are also the stages for which the average convective precipitation fraction is the highest according to the DPR precipitation type classification. Past studies have consistently shown the tendency of precipitation retrievals from passive radiometric measurements to underestimate precipitation intensity in convective areas over land [Henderson et al. 2017, Petković et al. 2019, Pfreundschuh et al. 2023]. The underestimation of precipitation intensity at the early stages of the life cycle of convective systems, i.e. their growing stages, when the convective activity is at its maximum, is therefore unsurprising. While this bias tendency is expected to generalize to most of the convective systems over land globally, its relative magnitude likely locally depends on the specific nature of convection, and may vary with regions, seasons and synoptic climate and weather conditions [Houze et al. 2015, Sullivan et al. 2019, Schumacher and Funk 2023].

Over ocean (Central Atlantic and Gulf of Guinea) the biases of GMI-GPROF against CORRA are much smaller than over land, the main noticeable pattern being a slight negative bias for short-lived

systems and a slight positive bias for long-lived systems. It must be noted that the GPROF algorithm is trained differently over different surface types. The GPROF training process has indeed been repeated for each one of the 14 surface classes accounted for by the algorithm, with a unique a-priori database used for each class [Randel et al. 2020]. Over ocean, the low-frequency radiances (below 30 GHz) measured by passive microwave imagers closely relate to the emission by liquid rain drops in the lower atmospheric levels, and are therefore good predictors of near-surface precipitation intensity, allowing accurate estimation with low biases from passive measurements. Over land the low-frequency microwave atmospheric signal is entangled with the spatially and temporally variable emission signal from the surface, making the interpretation of radiances measured at the top of the atmosphere much more ambiguous [Turk et al. 2021].

While only estimates from GMI are compared to CORRA retrievals in the present study, one may expect that passive microwave retrievals from similar instruments, such as the AMSR-2 and SSMI-S radiometers, show similar systematic biases. Unfortunately, coincident observations of the DPR with these other passive microwave radiometers are too sparse to perform such a detailed bias analysis with required statistical robustness (unlike for GMI and DPR which are onboard the same platform). Ultimately, the biases of the level-2 passive microwave retrievals are likely to propagate into level-3 products such as IMERG.

4.3 Including GEO-tracking information in future passive microwave retrievals of precipitation for improved accuracy

With the present study we assessed the potential information provided by the GEO infrared regarding the "history" of individual cloud systems, through cloud tracking. The results presented here demonstrate that the information derived from the GEO infrared cloud tracking algorithm TOOCAN can to a certain degree be used to predict the biases and errors of passive microwave precipitation retrievals. Indeed, we show that the development stage of a convective cloud system is a strong statistical indicator of the intensity of convection, which itself strongly influences the sign and magnitude of biases and errors in passive precipitation estimates. While estimates of the convective fraction of cloud systems generally rely on the availability of radar observation, the cloud development stage can be computed anytime and anywhere using global GEO cloud tracking. Allowing precipitation retrieval algorithms to utilize this information has the potential to improve the accuracy of passive satellite precipitation retrievals. In its future versions (8 and beyond), the GPROF algorithm will migrate toward a deep convolutional neural network retrieval approach instead of the current Bayesian *k*-nearest neighbor algorithm [Pfreundschuh et al., 2022, 2023]. The deep learning framework offers the possibility to add any number of ancillary variables as predictors (without having to rely on a-priori classification, or segment the training database, or perform multiple training/parameter regression under different environmental conditions). The results of the present study advocate for including information derived from GEO cloud-tracking, such as cloud systems' age or development stage, as inputs of deep learning algorithms for the remote sensing of precipitation. Our results also advocate for continuing the development of GEO cloud tracking algorithms

toward operational real-time / short-latency algorithms and products. The high homogeneity of all the computed stage-dependent statistics across the different land regions on one side, and across the two oceanic regions on the other side, and across systems of different life duration, is also a positive indicator regarding the potential global predictive power of the cloud-tracking information.

The cloud development stage, besides being a good statistical predictor of systematic biases in passive microwave retrievals (and thus being potentially usable for bias correction), is also a good predictor of the average magnitude (in absolute value) of the random errors. The cloud development stage information could therefore also be utilized for uncertainty quantification, for the purpose of systematically providing a measure of uncertainty/accuracy along with each estimated value in satellite QPE products [Guilloteau et al. 2022].

Data availability

All datasets used in these study are publicly available for research: the TOOCAN data at https://doi.org/10.14768/20191112001.1, the CORRA data at https://doi.org/10.5067/GPM/DPRGMI/CMB/2B/07, and the GMI GPROF data at https://doi.org/10.5067/GPM/GMI/GPM/GPROF/2A/07.

References

Ai, Y., Li, W., Meng, Z. and Li, J., 2016. Life cycle characteristics of MCSs in middle east China tracked by geostationary satellite and precipitation estimates. Monthly Weather Review, 144(7), pp.2517-2530, doi:10.1175/MWR-D-15-0197.1.

Biasutti, M., Battisti, D.S. and Sarachik, E.S., 2004. Mechanisms controlling the annual cycle of precipitation in the tropical Atlantic sector in an atmospheric GCM. Journal of climate, 17(24), pp.4708-4723, doi:10.1175/JCLI-3235.1.

Biasutti, M., 2019. Rainfall trends in the African Sahel: Characteristics, processes, and causes. Wiley Interdisciplinary Reviews: Climate Change, 10(4), p.e591, doi: 10.1002/wcc.591.

Bouniol, D., Roca, R., Fiolleau, T. and Poan, D.E., 2016. Macrophysical, microphysical, and radiative properties of tropical mesoscale convective systems over their life cycle. Journal of Climate, 29(9), pp.3353-3371, doi:10.1175/JCLI-D-15-0551.1.

Berthet, S., Roca, R., Duvel, J.P. and Fiolleau, T., 2017. Subseasonal variability of mesoscale convective systems over the tropical northeastern Pacific. Quarterly Journal of the Royal Meteorological Society, 143(703), pp.1086-1094, doi:10.1002/qj.2992.

Cui, W., Dong, X., Xi, B., Feng, Z.H.E. and Fan, J., 2020. Can the GPM IMERG final product accurately represent MCSs' precipitation characteristics over the central and eastern United States?. Journal of Hydrometeorology, 21(1), pp.39-57, doi:10.1175/JHM-D-19-0123.1.

Elsaesser, G.S., Roca, R., Fiolleau, T., Del Genio, A.D. and Wu, J., 2022. A simple model for tropical convective cloud shield area growth and decay rates informed by geostationary IR, GPM, and Aqua/AIRS satellite data. Journal of Geophysical Research: Atmospheres, 127(10), p.e2021JD035599, doi: 10.1029/2021JD035599.

Escrig, H., Batlles, F.J., Alonso, J., Baena, F.M., Bosch, J.L., Salbidegoitia, I.B. and Burgaleta, J.I., 2013. Cloud detection, classification and motion estimation using geostationary satellite imagery for cloud cover forecast. Energy, 55, pp.853-859, doi:10.1016/j.energy.2013.01.054.

Farnsworth, A., White, E., Williams, C.J., Black, E. and Kniveton, D.R., 2011. Understanding the large scale driving mechanisms of rainfall variability over Central Africa. In African climate and climate change: physical, social and political perspectives, Springer, pp.101-122, doi:10.1007/978-90-481-3842-5_5.

Feng, Z., Leung, L.R., Liu, N., Wang, J., Houze Jr, R.A., Li, J., Hardin, J.C., Chen, D. and Guo, J., 2021. A global high-resolution mesoscale convective system database using satellite-derived cloud tops, surface precipitation, and tracking. Journal of Geophysical Research: Atmospheres, 126(8), p.e2020JD034202, doi:10.1029/2020JD034202.

Feng, Z., Hardin, J., Barnes, H.C., Li, J., Leung, L.R., Varble, A. and Zhang, Z., 2023. PyFLEXTRKR: a flexible feature tracking Python software for convective cloud analysis. Geoscientific Model Development, 16(10), pp.2753-2776, doi:10.5194/gmd-16-2753-2023.

Fiolleau, T. and Roca, R., 2013, A. An algorithm for the detection and tracking of tropical mesoscale convective systems using infrared images from geostationary satellite. IEEE transactions on Geoscience and Remote Sensing, 51(7), pp.4302-4315, doi:10.1109/TGRS.2012.2227762.

Fiolleau, T. and Roca, R., 2013, B. Composite life cycle of tropical mesoscale convective systems from geostationary and low Earth orbit satellite observations: Method and sampling considerations. Quarterly Journal of the Royal Meteorological Society, 139(673), pp.941-953, doi:.10.1002/qj.2174.

Garreaud, R.D., Vuille, M., Compagnucci, R. and Marengo, J., 2009. Present-day south american climate. Palaeogeography, Palaeoclimatology, Palaeoecology, 281(3-4), pp.180-195, doi: 10.1016/j.palaeo.2007.10.032.

Gorooh, V.A., Asanjan, A.A., Nguyen, P., Hsu, K. and Sorooshian, S., 2022. Deep neural network high SpatioTEmporal resolution precipitation estimation (Deep-STEP) using passive microwave and infrared data. Journal of Hydrometeorology, 23(4), pp.597-617, doi:10.1175/JHM-D-21-0194.1.

Grecu, M., Olson, W.S., Munchak, S.J., Ringerud, S., Liao, L., Haddad, Z., Kelley, B.L. and McLaughlin, S.F., 2016. The GPM combined algorithm. Journal of Atmospheric and Oceanic Technology, 33(10), pp.2225-2245, doi:10.1175/JTECH-D-16-0019.1.

Gu, G. and Adler, R.F., 2004. Seasonal evolution and variability associated with the West African monsoon system. Journal of climate, 17(17), pp.3364-3377, doi:10.1175/1520-0442(2004)017<3364:SEAVAW>2.0.CO;2.

Gu, G. and Adler, R.F., 2006. Interannual rainfall variability in the tropical Atlantic region. Journal of Geophysical Research: Atmospheres, 111(D2), doi:10.1029/2005JD005944.

Guilloteau, C., Foufoula-Georgiou, E. and Kummerow, C.D., 2017. Global multiscale evaluation of satellite passive microwave retrieval of precipitation during the TRMM and GPM eras: Effective resolution and regional diagnostics for future algorithm development. Journal of Hydrometeorology, 18(11), pp.3051-3070, doi:10.1175/JHM-D-17-0087.1

Guilloteau, C., Foufoula-Georgiou, E., Kirstetter, P., Tan, J. and Huffman, G.J., 2021. How well do multisatellite products capture the space–time dynamics of precipitation? Part I: Five products assessed via a wavenumber–frequency decomposition. Journal of Hydrometeorology, 22(11), pp.2805-2823, doi:10.1175/JHM-D-21-0075.1.

Guilloteau, C., Foufoula-Georgiou, E., Kirstetter, P., Tan, J. and Huffman, G.J., 2022. How Well Do Multisatellite Products Capture the Space–Time Dynamics of Precipitation? Part II: Building an Error Model through Spectral System Identification. Journal of Hydrometeorology, 23(9), pp.1383-1399, doi:10.1175/JHM-D-22-0041.1.

Guilloteau, C., Le, P.V. and Foufoula-Georgiou, E., 2023. Constraining the multiscale structure of geophysical fields in machine-learning: the case of precipitation. IEEE Geoscience and Remote Sensing Letters, 20, pp.1-5, doi:10.1109/LGRS.2023.3284278.

Hanel, R.A., Licht, J., Nordberg, W., Stampfl, R.A. and Stroud, W.G., 1960. The satellite Vanguard II: cloud cover experiment. IRE Transactions on Military Electronics, (2/3), pp.245-247, doi:10.1109/IRET-MIL.1960.5008229.

Henderson, D.S., Kummerow, C.D., Marks, D.A. and Berg, W., 2017. A regime-based evaluation of TRMM oceanic precipitation biases. Journal of Atmospheric and Oceanic Technology, 34(12), pp.2613-2635, doi:10.1175/JTECH-D-16-0244.1.

Hou, A.Y., Kakar, R.K., Neeck, S., Azarbarzin, A.A., Kummerow, C.D., Kojima, M., Oki, R., Nakamura, K. and Iguchi, T., 2014. The global precipitation measurement mission. Bulletin of the American meteorological Society, 95(5), pp.701-722, doi:10.1175/BAMS-D-13-00164.1.

Houze Jr, R.A., Rasmussen, K.L., Zuluaga, M.D. and Brodzik, S.R., 2015. The variable nature of convection in the tropics and subtropics: A legacy of 16 years of the Tropical Rainfall Measuring Mission satellite. Reviews of Geophysics, 53(3), pp.994-1021, doi:10.1002/2015RG000488.

Kidd, C., Huffman, G., Maggioni, V., Chambon, P. and Oki, R., 2021. The global satellite precipitation constellation: Current status and future requirements. Bulletin of the American Meteorological Society, 102(10), pp.E1844-E1861, doi:10.1175/BAMS-D-20-0299.1.

Li, R., Guilloteau, C., Kirstetter, P.E. and Foufoula-Georgiou, E., 2023. How well does the IMERG satellite precipitation product capture the timing of precipitation events?. Journal of Hydrology, 620, p.129563, doi:10.1016/j.jhydrol.2023.129563.Marengo, J.A. and Nobre, C.A., 2001. Climate in the Amazon Basin and its Links to the Global Climate System. In The biogeochemistry of the Amazon basin, Oxford University Press, pp.17-41.

NASA, 2021. Data Processing Levels. https://www.earthdata.nasa.gov/engage/open-data-services-and-software/data-information-policy/data-levels.

Nicholson, S.E., 2018. Climate of the Sahel and West Africa. In Oxford Research Encyclopedia of Climate Science, doi:10.1093/acrefore/9780190228620.013.510.

Petković, V., Orescanin, M., Kirstetter, P., Kummerow, C. and Ferraro, R., 2019. Enhancing PMW satellite precipitation estimation: Detecting convective class. Journal of Atmospheric and Oceanic Technology, 36(12), pp.2349-2363, doi:10.1175/JTECH-D-19-0008.1.

Pfreundschuh, S., Brown, P.J., Kummerow, C.D. and Eriksson, P., 2022. GPROF-NN: a neural-network-based implementation of the Goddard Profiling Algorithm. Atmospheric Measurement Techniques, 15(17), pp.5033-5060, doi:10.5194/amt-15-5033-2022.

Pfreundschuh, S., Guilloteau, C., Brown, P.J., Kummerow, C.D. and Eriksson, P., 2023. GPROF V7 and beyond: Assessment of current and potential future versions of the GPROF passive microwave precipitation retrievals against ground radar measurements over the continental US and the Pacific Ocean. EGUsphere, 2023, pp.1-33, doi:10.5194/egusphere-2023-1310.

Randel, D.L., Kummerow, C.D. and Ringerud, S., 2020. The Goddard Profiling (GPROF) precipitation retrieval algorithm. Satellite Precipitation Measurement: Volume 1, pp.141-152, doi:10.1007/978-3-030-24568-9_8.

Roca, R., Aublanc, J., Chambon, P., Fiolleau, T. and Viltard, N., 2014. Robust observational quantification of the contribution of mesoscale convective systems to rainfall in the tropics. Journal of Climate, 27(13), pp.4952-4958, doi:10.1175/JCLI-D-13-00628.1.

Roca, R., Fiolleau, T. and Bouniol, D., 2017. A simple model of the life cycle of mesoscale convective systems cloud shield in the tropics. Journal of Climate, 30(11), pp.4283-4298, doi:10.1175/JCLI-D-16-0556.1.

Roca, R. and Fiolleau, T., 2020. Extreme precipitation in the tropics is closely associated with long-lived convective systems. Communications Earth & Environment, 1(1), p.18, 10.1038/s43247-020-00015-4.

Schumacher, C. and Funk, A., 2023. Assessing convective-stratiform precipitation regimes in the tropics and extratropics with the GPM satellite radar. Geophysical Research Letters, 50(14), doi:10.1029/2023GL102786.

Smith, E.A. and Phillips, D.R., 1972. Automated cloud tracking using precisely aligned digital ATS pictures. IEEE Transactions on computers, 100(7), pp.715-729, doi:10.1109/T-C.1972.223574.

Sullivan, S.C., Schiro, K.A., Stubenrauch, C. and Gentine, P., 2019. The response of tropical organized convection to El Niño warming. Journal of Geophysical Research: Atmospheres, 124(15), pp.8481-8500, doi:10.1029/2019JD031026.

Turk, F.J., Ringerud, S.E., You, Y., Camplani, A., Casella, D., Panegrossi, G., Sanò, P., Ebtehaj, A., Guilloteau, C., Utsumi, N. and Prigent, C., 2021. Adapting passive microwave-based precipitation algorithms to variable microwave land surface emissivity to improve precipitation estimation from the GPM constellation. Journal of Hydrometeorology, 22(7), pp.1755-1781, doi: 10.1175/JHM-D-20-0296.1.

Wolf, D.E., Hall, D.J. and Endlich, R.M., 1977. Experiments in automatic cloud tracking using SMS-GOES data. Journal of Applied Meteorology and Climatology, 16(11), pp.1219-1230, doi:10.1175/1520-0450(1977)016<1219:EIACTU>2.0.CO;2.